

1-27-2017

Numerical Modeling of a Multiscale Gravity Wave Event and Its Airglow Signatures over Mount Cook, New Zealand, During the DEEPWAVE Campaign

C. J. Heale

Embry-Riddle Aeronautical University, HEALEC@erau.edu

K. Bossert

GATS Inc.

J. B. Snively

Embry-Riddle Aeronautical University, snivelyj@erau.edu

D. C. Fritts

GATS Inc.

P. -D. Pautet

Utah State University

See next page for additional authors

Follow this and additional works at: <https://commons.erau.edu/publication>



Part of the [Atmospheric Sciences Commons](#)

Scholarly Commons Citation

Heale, C. J., K. Bossert, J. B. Snively, D. C. Fritts, P.-D. Pautet, and M. J. Taylor (2017), Numerical modeling of a multiscale gravity wave event and its airglow signatures over Mount Cook, New Zealand, during the DEEPWAVE campaign, *J. Geophys. Res. Atmos.*, 122, 846–860, doi:10.1002/2016JD025700

This Article is brought to you for free and open access by Scholarly Commons. It has been accepted for inclusion in Publications by an authorized administrator of Scholarly Commons. For more information, please contact commons@erau.edu.

Authors

C. J. Heale, K. Bossert, J. B. Snively, D. C. Fritts, P. -D. Pautet, and M. J. Taylor

RESEARCH ARTICLE

10.1002/2016JD025700

Key Points:

- A 2-D nonlinear, compressible model is used to investigate a large-amplitude, multiscale mountain wave event
- Small-scale waves and vortices are generated in situ by a breaking mountain wave, consistent with observations
- There is a preference for instability to appear most prominent in the warm phase front of the mountain wave

Correspondence to:

C. J. Heale,
healec@erau.edu

Citation:

Heale, C. J., K. Bossert, J. B. Snively, D. C. Fritts, P.-D. Pautet, and M. J. Taylor (2017), Numerical modeling of a multiscale gravity wave event and its airglow signatures over Mount Cook, New Zealand, during the DEEPWAVE campaign, *J. Geophys. Res. Atmos.*, 122, 846–860, doi:10.1002/2016JD025700.

Received 25 JUL 2016

Accepted 5 JAN 2017

Accepted article online 9 JAN 2017

Published online 27 JAN 2017

Numerical modeling of a multiscale gravity wave event and its airglow signatures over Mount Cook, New Zealand, during the DEEPWAVE campaign

C. J. Heale¹ , K. Bossert² , J. B. Snively¹ , D. C. Fritts² , P.-D. Pautet³ , and M. J. Taylor³

¹Department of Physical Sciences, Embry-Riddle Aeronautical University, Daytona Beach, Florida, USA, ²GATS Inc., Boulder, Colorado, USA, ³Center for Atmospheric and Space Sciences, Utah State University, Logan, Utah, USA

Abstract A 2-D nonlinear compressible model is used to simulate a large-amplitude, multiscale mountain wave event over Mount Cook, NZ, observed as part of the Deep Propagating Gravity Wave Experiment (DEEPWAVE) campaign and to investigate its observable signatures in the hydroxyl (OH) layer. The campaign observed the presence of a $\lambda_x = 200$ km mountain wave as part of the 22nd research flight with amplitudes of >20 K in the upper stratosphere that decayed rapidly at airglow heights. Advanced Mesospheric Temperature Mapper (AMTM) showed the presence of small-scale (25–28 km) waves within the warm phase of the large mountain wave. The simulation results show rapid breaking above 70 km altitude, with the preferential formation of almost-stationary vortical instabilities within the warm phase front of the mountain wave. An OH airglow model is used to identify the presence of small-scale wave-like structures generated in situ by the breaking of the mountain wave that are consistent with those seen in the observations. While it is easy to interpret these features as waves in OH airglow data, a considerable fraction of the features are in fact instabilities and vortex structures. Simulations suggest that a combination of a large westward perturbation velocity and shear, in combination with strong perturbation temperature gradients, causes both dynamic and convective instability conditions to be met particularly where the wave wind is maximized and the temperature gradient is simultaneously minimized. This leads to the inevitable breaking and subsequent generation of smaller-scale waves and instabilities which appear most prominent within the warm phase front of the mountain wave.

1. Introduction

Gravity waves are understood to play a crucial role in the transfer of energy and momentum from lower atmospheric sources to the mesosphere and lower thermosphere (MLT) region [Hung and Kuo, 1978; Lindzen, 1981; Holton, 1982; Vincent and Reid, 1983; Fritts and Dunkerton, 1985; Fritts and Vincent, 1987; Kelley, 1997; Hocke and Tsuda, 2001; Fritts and Alexander, 2003]. Air flow over topography and convective processes such as thunderstorms, weather fronts, and shears provide efficient sources for gravity wave generation [Fritts and Alexander, 2003, and references cited within]. Through physical mechanisms such as breaking, dissipation, and critical level filtering, gravity waves have the ability to cause momentum and energy deposition into the upper atmosphere and influence mean temperatures and winds [Pitteway and Hines, 1963; Lindzen, 1981; Holton, 1982, 1983; Fritts, 1984; Fritts et al., 1996, 2006; Vadas and Fritts, 2006; Vadas, 2007; Yiğit et al., 2008, 2009; Vadas and Liu, 2009; Fritts and Lund, 2011; Waterscheid and Hickey, 2011; Hickey et al., 2011; Vadas and Liu, 2013; Heale et al., 2014a, 2014b]. One such manifestation of this is the reversal of the mesospheric jets and the cold summer mesopause [Lindzen, 1981; Holton, 1982, 1983; Garcia and Solomon, 1985; Lübken et al., 1999; Fritts and Alexander, 2003; Fritts et al., 2006]; thus, understanding the effects of gravity waves on the MLT is necessary for more accurate general circulation models and predictions.

Numerous studies have been performed to quantify the momentum flux due to gravity waves [Fritts and Vincent, 1987; Tsuda et al., 1990; Hitchman et al., 1992; Nakamura et al., 1993; Fritts and Lu, 1993; Swenson et al., 1999; Espy et al., 2006; Gardner and Liu, 2007], and many suggest that small-scale waves (10–100 km wavelength) with high phase speeds are likely to have the largest influences in the MLT region [Vincent and Reid, 1983; Fritts and Vincent, 1987; Fritts et al., 2014]. However, large-amplitude gravity waves can cascade into other scales [e.g., Klostermeyer, 1991; Fritts et al., 2009; Lund and Fritts, 2012], and it can be unclear in airglow and

lidar studies whether small-scale structures are indeed propagating gravity waves or the result of in situ generated instabilities or “ripples” [Taylor *et al.*, 1997; Nakamura *et al.*, 1999; Hecht, 2004]. Observations have also revealed unstable or nearly unstable layers which are a few kilometers in depth, suggesting the presence of unstable gravity waves with similar vertical wavelengths and convective “folds” that are approximately equal to the convective layer depth [e.g., Lübken, 1997; Hoppe *et al.*, 1999].

Gravity wave breaking can also cause a “self-acceleration” feedback mechanism whereby the breaking waves accelerate the mean wind, leading to a larger shear and more critical level filtering, which in turn can cause more wave breaking and dissipation. This can also act to confine instability to the shear layer that generates it [Franke and Robinson, 1999; Dosser and Sutherland, 2011; Lund and Fritts, 2012; Liu *et al.*, 2014; Fritts *et al.*, 2015]. This mechanism is not accounted for by linear theory, and capturing all turbulent scales accurately over long time scales requires 3-D direct numerical simulations [Andreassen *et al.*, 1994; Fritts *et al.*, 2009]. However, these studies are currently computationally prohibitive for larger-scale waves.

While instrumentation is used to measure the background atmosphere and the waves that propagate through it, instruments are limited by spatial and temporal resolution, sensitivity, and field of view requiring comprehensive multi-instrument observations. The Deep Propagating Gravity Wave Experiment (DEEPWAVE) was conceived to measure wave propagation and characterize the propagation environment from the ground to 100 km altitude [Fritts *et al.*, 2016]. This was done using a suite of instruments concurrently on the ground and aboard two aircraft, each of which covered a different altitude range and horizontal extent. The airborne program occurred from 6 June to 21 July 2014 over the known gravity wave hotspots of New Zealand and Tasmania and was primarily concerned with the study of orographically forced gravity waves. Orographically forced waves are those formed by the flow of wind over terrain and are also known as mountain waves. They are quasi-stationary (i.e., their ground relative frequency is approximately zero) and can only propagate if there is a background wind present; otherwise, the wave encounters a critical level.

During the 22nd research flight (RF22) on 13 July 2014, a large-amplitude, multiscale gravity wave environment was observed over Mount Cook, New Zealand. Bossert *et al.* [2015] characterized the variability, scales, amplitudes, phase speeds, and momentum fluxes of this environment. This consisted of a 200 km horizontal wavelength stationary mountain wave which decreased rapidly in amplitude above 85 km altitude, along with the presence of smaller-scale waves found predominately within the warm phase of the mountain wave. As had been suggested by previous literature [e.g., Fritts *et al.*, 2014; Espy *et al.*, 2004], the smaller-scale waves possessed momentum flux values that were greater than those of the larger-scale wave. This study raised three important questions about multiscale gravity wave environments that we aim to address in this modeling study.

1. What mechanism causes the rapid decrease in amplitude above 85 km, and how does this manifest itself for stationary mountain waves?
2. Why do the small-scale waves appear to have a preference for the warm phase front of the larger-scale wave?
3. Can the apparent small-scale waves seen in the data be explained by in situ generation by the larger-scale wave?

In this study, we use a 2-D nonlinear gravity wave model [Snively and Pasko, 2008] to simulate a quasi-stationary wave in a realistic background atmosphere specified to match data from Bossert *et al.* [2015]. We aim to answer the questions laid out above using the model results including calculations of the OH airglow response [e.g., Snively *et al.*, 2010; Snively, 2013]. The paper is organized as follows: section 2 will briefly describe the data and results from Bossert *et al.* [2015], section 3 describes the model setup, wave forcing, and the background atmosphere and provides a comparison between the lidar and model results below 60 km, sections 4–6 will answer each of the questions posed above, and finally, section 7 will provide discussion and conclusions.

2. Overview of the Data

The data for the Bossert *et al.* [2015] study was collected during four successive east-west flight paths aboard the National Science Foundation/National Centre for Atmospheric Research Gulfstream V research aircraft on 13 July 2014 as part of Research Flight 22 (RF22). The AMTM provided OH (3,1) emission data at zenith, with two wing cameras providing additional OH airglow imagery. A Rayleigh lidar provided temperature data from

Table 1. Temperature Measurements of the Larger-Scale Mountain Wave From *Bossert et al.* [2015]

T' (Large Wave, K)	Altitude (km)	Instrument
20	55	Rayleigh lidar
12–24	83	Sodium lidar
6–8	84	AMTM

20 to 60 km, while a sodium (Na) lidar provided sodium mixing ratios between 75 and 95 km. Background temperature and wind data were measured using a nearby Rayleigh lidar at Lauder, NZ, and a meteor radar at Kingston, Tasmania, respectively. Lower atmospheric background winds were estimated by the European Centre for Medium-Range Weather Forecasts (ECMWF).

2.1. Larger-Scale Wave

The 200 km quasi-stationary larger-scale mountain wave (~ 240 km horizontal wavelength when measured along the E-W flight path) had a westward intrinsic phase speed (opposite to the mean zonal wind), of approximately 24 m/s at 87 km altitude. Temperature amplitudes were estimated to be ~ 20 K at 55 km altitude from the Rayleigh lidar, between 12 and 24 K near 83 km altitude from the Sodium lidar (inferred from vertical displacements of sodium mixing ratios) and between 6 and 8 K near 84 km altitude from the AMTM. There is strong evidence of wave dissipation above 85 km and a suggested critical level around 90 km. The estimated upper bounds on the momentum fluxes were 96, 52, and $9 \text{ m}^2 \text{ s}^{-2}$ for altitudes of 83, 84, and 87 km, respectively. The large-scale wave parameters are summarized in Table 1.

2.2. Smaller-Scale Waves

Bossert et al. [2015] presented four specific cases of small-scale waves identified in the AMTM data. Their horizontal wavelengths varied from 25 to 28 km, and all were predominately aligned with the larger-scale wave. The first and third passes revealed gravity waves propagating to the east (in the direction of the background wind) at observed phase speeds of 100 and 130 m/s with perturbation temperatures of 7 and 5 K, respectively. The second pass revealed a wave which was measured to advect with the speed of the background wind and that could indicate an instability associated with the larger-scale wave. The fourth pass suggested another small-scale stationary wave which had a ground relative phase speed of zero and an amplitude of 4.4 K. It was noted that all four of these occurrences accompanied the warmer phase of the larger-scale mountain wave. The small-scale wave parameters are summarized in Table 2.

3. Model Setup and Background Atmosphere

3.1. Model Description

The numerical model solves the 2-D nonlinear, fully compressible Euler equations, with gravity as a balanced source term, and Navier Stokes viscosity [*Snively and Pasko, 2008; Snively, 2013*]. This is done using an adaptation of the Clawpack routines [<http://www.clawpack.org>], which solve a hyperbolic system of equations using a finite volume approach [*LeVeque, 2002; LeVeque and Berger, 2004*]. The model decomposes flux differences between cell boundaries into characteristic “*f waves*” [*Bale et al., 2002*], each of which propagate at characteristic speeds. The model accounts for dissipation due to molecular viscosity and thermal conduction and solves for these using a time-split method.

The compressible dynamics solution is also coupled to a model describing OH airglow photochemistry. Thus, it can simulate intensity and brightness-weighted temperature responses to gravity waves by the airglow layer [*Snively et al., 2010; Snively, 2013*].

Table 2. Small-Scale Wave Parameters Observed With the Airglow Cameras From *Bossert et al.* [2015]

Pass	T' (K)	c_p (m/s ⁻¹)	λ_h (km)
1	7	100 east	28
2	6	24 east	28
3	5	135 east	28
4	4.4	0	25

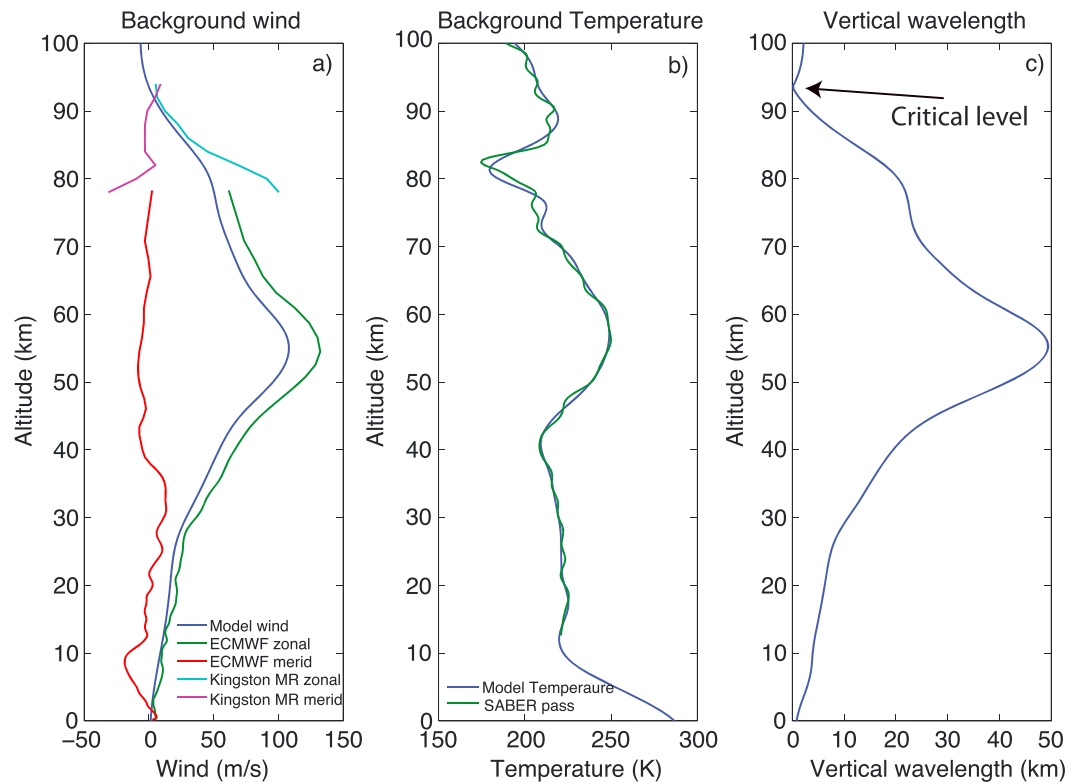


Figure 1. The background wind, temperature and resulting vertical wavelength profiles used for the simulations.

3.2. Background Atmosphere

The background atmosphere temperature (Figure 1b) was specified using a smoothed version of the Sounding of the Atmosphere using Broadband Emission Radiometry (SABER) data, presented in *Bossert et al.* [2015], between 10 and 100 km altitude. An NRLMSISE-00 profile [*Picone et al.*, 2002], set to Mount Cook, New Zealand (43°S, 170°E) on 13 July 2014 was used for altitudes from 0 to 10 km and 100 to 300 km. While the flight path was east-west, the mountain wave itself had a propagation direction ~60° east of north; therefore, the wind profile was specified to be along this direction. A smoothed version of the ECMWF forecast was used for the model winds from ground up to 73 km altitude. Above this, the wind was specified using a combination of the Kingston Meteor Radar data between 83 and 90 km and a HWM07 zonal wind profile [*Drob et al.*, 2008] set to the same parameters as the NRLMSISE-00 profile. The ECMWF, Kingston MR, and HWM07 profiles were merged and smoothed to create the final background wind profile (Figure 1a).

Based upon the wind and temperature data, the vertical wavelength of the larger-scale wave is calculated using the anelastic dispersion relation [*Gossard and Hooke*, 1975]

$$m^2 = \frac{k^2 N^2}{(\omega - kU)^2} - k^2 - \frac{1}{4H^2}, \quad (1)$$

where m is the vertical wave number, N is the buoyancy frequency, ω is the ground relative frequency (0 in this case), k is the horizontal wave number ($2\pi/200$ km), U is the background wind, and H is the scale height. The resulting plot is shown in Figure 1c.

The large wind (~110 m/s) at 55 km altitude refracts the wave to large vertical wavelengths (~50 km). At airglow heights, the vertical wavelength is much smaller at ~10 km, and a predicted critical level exists at $z = 93$ km.

3.3. Domain and Wave Forcing

The model domain ranged from -1500 to 1500 km in the horizontal direction and 300 km in the vertical direction with a 0.5 km resolution in both directions. Frames were output every 60 s and the simulation was run to $t = 16$ h. The bottom boundary was specified to be closed (reflective) at the ground and open at the side

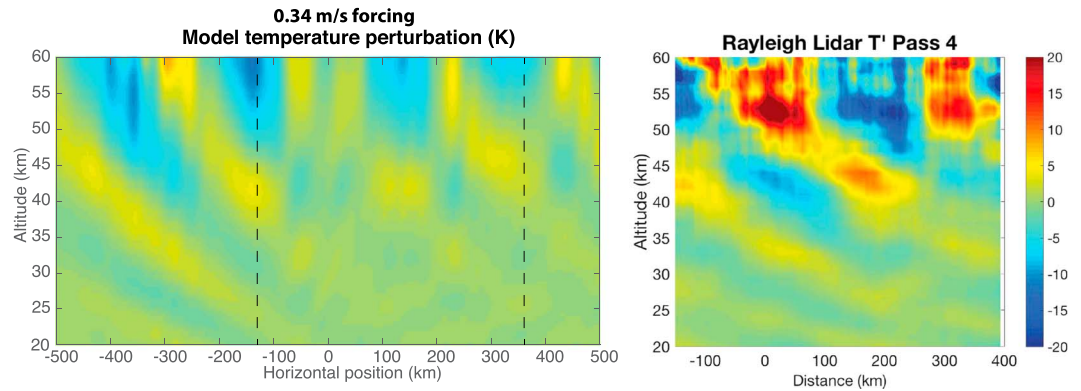


Figure 2. Comparison between (left) the model perturbation temperature results with $x=0$ representing the center of the forcing in the model, and (right) the Rayleigh Lidar data from RF22, reprinted from *Bossert et al.* [2015] where $x=0$ represents the location of Mt. Cook in the Lidar data.

and top boundaries. A numerical sponge layer was applied above 250 km altitude, although we only consider simulation results up 100 km altitude, which is near the highest altitude measured by the lidar instrument.

The larger-scale mountain wave was specified using a vertical body forcing centered at $x = 0$ km, $z = 10$ km. A mountain wave is approximated in the model by using a fixed phase structure in x and z with an amplitude that follows a Gaussian shape in time. Peak forcing occurs at $t = t_c$. The vertical body forcing is specified by

$$F(x, z, t) = A \cdot \rho \cdot \cos[k(x - x_c)] \cdot \exp \left[-\frac{(z - z_c)^2}{2\sigma_z^2} - \frac{(x - x_c)^2}{2\sigma_x^2} - \frac{(t - t_c)^2}{2\sigma_t^2} \right] \quad (2)$$

where $A = 0.34$ m/s², ρ is the density, k is the horizontal wave number ($2\pi/200$ km), $z_c = 10$ km, $\sigma_z = 3$ km, $x_c = 0$ km, $\sigma_x = 250$ km, $t_c = 6$ h, and $\sigma_t = 1.5$ h. The vertical half width is chosen to be large enough to generate a coherent gravity wave and not so large that the ambient atmospheric conditions vary too rapidly over that scale. The temporal half width is chosen to roughly represent the intrinsic period of the wave. The horizontal wavelength was chosen as 200 km because this was the actual wavelength of the wave along the propagation direction. The aircraft lidar measured a horizontal wavelength of 240 km as it flew along an E-W trajectory. In order to compare with the lidar results, we reproject our simulation such that the x axis aligns with the E-W plane; thus, we also show an apparent 240 km horizontal wavelength mountain wave, consistent with data. Note that the horizontal position of the source changes as a result of this re-projection.

3.4. Model-Data Comparison

In order to ensure that the model produces results consistent with the observations of *Bossert et al.* [2015], we plot and compare the model results alongside the Rayleigh lidar data between 20 and 60 km altitude in Figure 2. The model result shown is the total temperature field minus the initial background temperature displayed in Figure 1b. The general phase structure is consistent with that of the data and both show 20 K peak amplitudes. However, there is a tendency for the model to show broader and larger-amplitude negative temperature perturbations than positive ones, and the presence of smaller horizontal structure, neither of which appears in the data at the resolution processed. It is also noted that the wave is present both west and east of the source in the simulation, whereas the lidar data in the stratosphere are shown east of the mountain, and data on the west side are not available.

4. Reduction in Amplitude of the Large-Scale Mountain Wave Via Rapid Breaking/Instability

4.1. Evolution of the Wave

Figure 3 shows the resulting simulation at four different times. At $t = 7$ h, the mountain wave is still propagating upward and relatively weak in the MLT region, but is preceded by a ~ 60 km structure (one fourth of the mountain wave horizontal scale) which is likely the result of nonlinear processes associated with the large amplitude of the forcing. At $t = 8.5$ h, the wave amplitudes have increased and there is a clear modulation of the 60 km structure by the mountain wave. Vortices begin to appear at $z = 85$ km altitude and a smaller

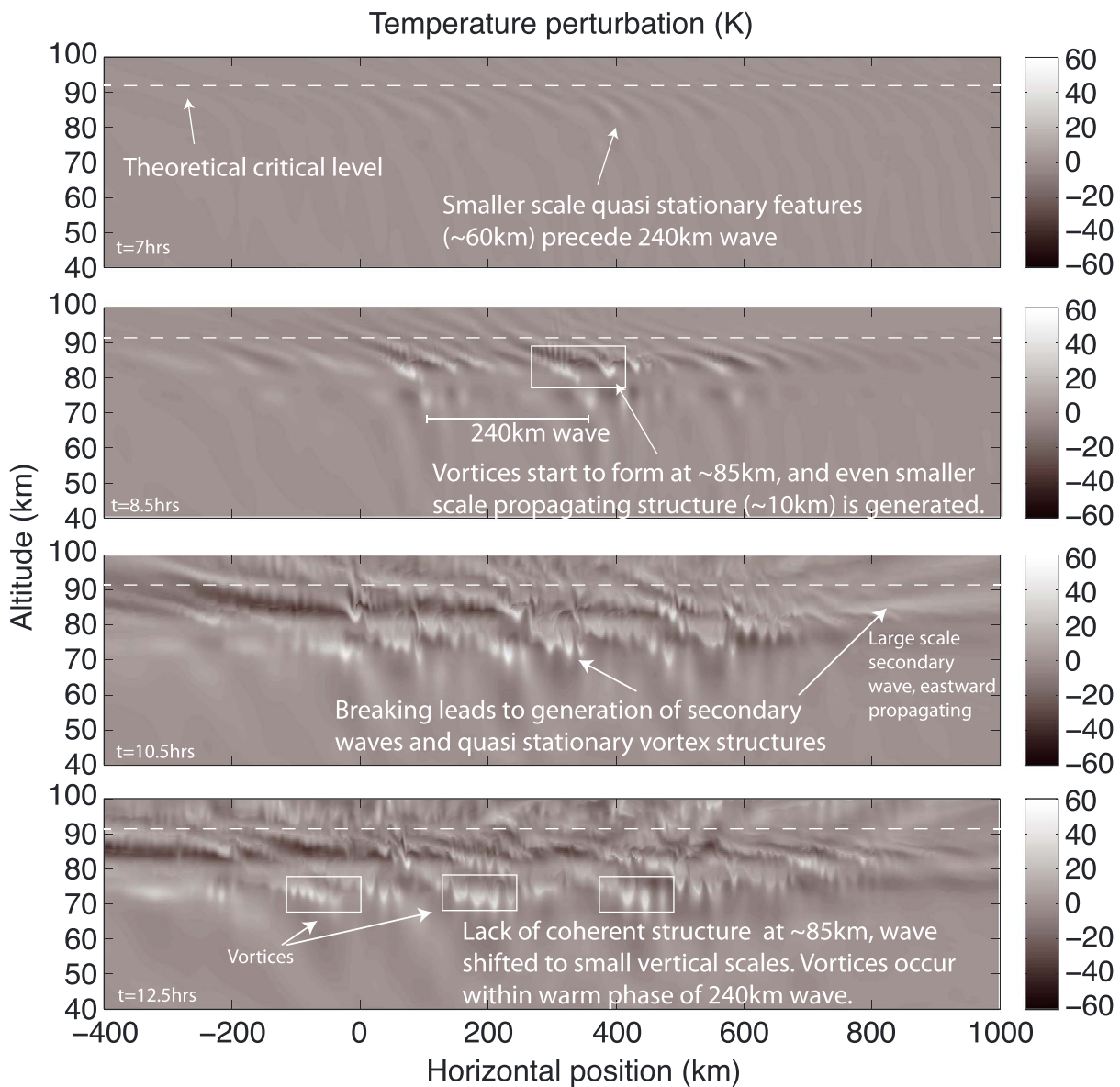


Figure 3. The simulation of the RF22 event, showing the perturbation temperature at four different times. The simulation shows the onset of breaking which creates 10km scale propagating structure initially. As time progresses, stationary vortex structures form as well as large and small-scale secondary features which propagate both eastward and westward. It becomes unclear at late times what features are actually a wave and what are instability feature that advect with the wave/background wind.

10 km propagating wave structure emerges also. There is also a layer of diminished wave amplitude just below 80 km, corresponding with a steep, but localized, background temperature decrease (see Figure 1c). By $t = 10.5$ h, the wave is rapidly breaking with clear small-scale structure appearing most evidently along the warm phase fronts. Amplitudes are peaking at ~ 60 K at an altitude of 70 km. The wave has evolved into a multiscale environment consisting of both eastward and westward propagating, and quasi-stationary structures. By $t = 12.5$ h, quasi-stationary vortices have formed above 70 km altitude, in a fixed pattern coinciding with the warm phase fronts of the mountain wave; amplitudes are similar to those at $t = 10.5$ h. While it is harder to discern a pattern above 80 km altitude, there is a clear shift to smaller vertical scales caused by the critical level; however, breaking and the generation of secondary features allow for propagation beyond the critical level. It is clear that this event is extremely complex and nonlinear, as a results of large amplitude. We note, however, that the simulation is only two dimensional and the effect of breaking in the third dimension is not

Table 3. Typical MW Wave Parameters From the Simulation at 55 km and 83 km Altitude

Altitude (km)	λ_x	C_p (ms ⁻¹)	C_{pl} (ms ⁻¹)	Amplitude (K)
55	240	-11	-115	15
83	243	-19	-56	20

taken into account; therefore, amplitudes of coherent features may be overestimated at later times. We will thus focus predominately upon the early stages of breaking and formation of 2-D instability features. Typical MW wave parameters from the simulation are displayed in Table 3.

4.2. Onset of Breaking

To better understand the nature of the wave instability, breaking, and associated mechanisms, we first assess the convective and dynamic stability criteria at the onset of breaking. The linear instability limit is approached as the wave's perturbation velocity (u') approaches the ground relative phase speed of the wave (i.e., $u' = u_0 + c_\phi$) [Fritts, 1984]. In the case of a stationary wave there is no ground relative phase speed; thus, the instability criteria are met when the perturbation velocity is equal to the intrinsic phase speed, which in turn equal to the negative of the background wind (i.e., $u' = c_{\phi_{int}} = -u_0$).

Convective instability in a fluid results from an inversion of density layers, while dynamic instability results from shear layers; both can be assessed using the Richardson (Ri) number:

$$Ri = \frac{N^2}{(du/dz)^2} \quad (3)$$

A fluid is said to be dynamically unstable if the Richardson number is between 0 and 0.25; thus, the shear is sufficient to overcome the static stability of the stratified fluid and Kelvin-Helmholtz instabilities can form. However, this is a necessary but not sufficient condition. If the Richardson number is negative, then the fluid is convectively unstable and overturning can commence, while shear may still play an important role.

To investigate the instabilities, we identify a horizontal location where breaking/instability first occurs before the flow becomes too disturbed; we then take a vertical cross section at this location and plot the intrinsic phase speed, perturbation velocity, and Richardson number as a function of altitude. Figure 4 shows the early stages of breaking over the course of 45 min. Figure 4 (left column) shows the temperature perturbation at four times with a vertical black line overlaid; this represents the location of the vertical cross section (shown in Figure 4 (right column)). Figure 4 (right column) shows the perturbation velocity, the wave intrinsic phase speed, and Richardson number (Ri) as a function of altitude. The linear instability criteria are met when the perturbation velocity (dark blue line) is more negative than the intrinsic phase speed (green line). The dynamic instability condition is met when Ri is between 0 and 0.25 (light blue vertical line) or the convective instability condition is met when Ri is negative. We note, however, that these are simplifying assumptions that do not necessarily hold for complex, distorted flows. These stability criteria were historically derived using normal mode analysis with a purely vertical stratification and horizontal velocity fields. Studies have found that instability can occur in gravity waves for values below these instability thresholds depending of the gravity wave parameters and amplitudes [e.g., Dunkerton, 1989; Sonmor and Klaassen, 1997; Fritts et al., 2006; Achatz, 2007; Fritts et al., 2009].

At $t = 8$ h, the westward perturbation velocity approaches and then exceed the intrinsic phase speed, while the Ri number is just above the 0.25 threshold. The wave appears stable and no breaking or instability is yet present. By $t = 8.25$ h the perturbation velocity has become stronger and the signs of an overturning region can be seen at ~ 83 km. The stronger perturbation velocity and the shift of the wave by the ambient atmosphere to smaller vertical scales has created a larger velocity shear and temperature gradient in this region, leading to the dynamic and linear instability criteria being met. At $t = 8.5$ h, small-scale structure has begun to form and overturning commences. The small-scale structure appears to originate at the location of the overturning with a 10 km horizontal scale, it propagates westward at the speed of the background wind and upward. By $t = 8.75$ h, vortical structures can be seen, the Ri number is negative indicating convective instability, and we note that the amplitude rapidly decays above 85 km altitude. The Ri minimum coincides with the maximum westward wind perturbation (indicated by horizontal black line), which corresponds to where the temperature gradient (dT/dz) is minimized (i.e., moving from the warm to the cold phase). The small-scale structure appears to have large vertical wavelengths and forms perpendicular to the phase fronts of the large-scale waves. Note that the altitude at which the linear instability condition is met has descended to 80 km. This is due to the upward propagation of the peak MW energy density with time.

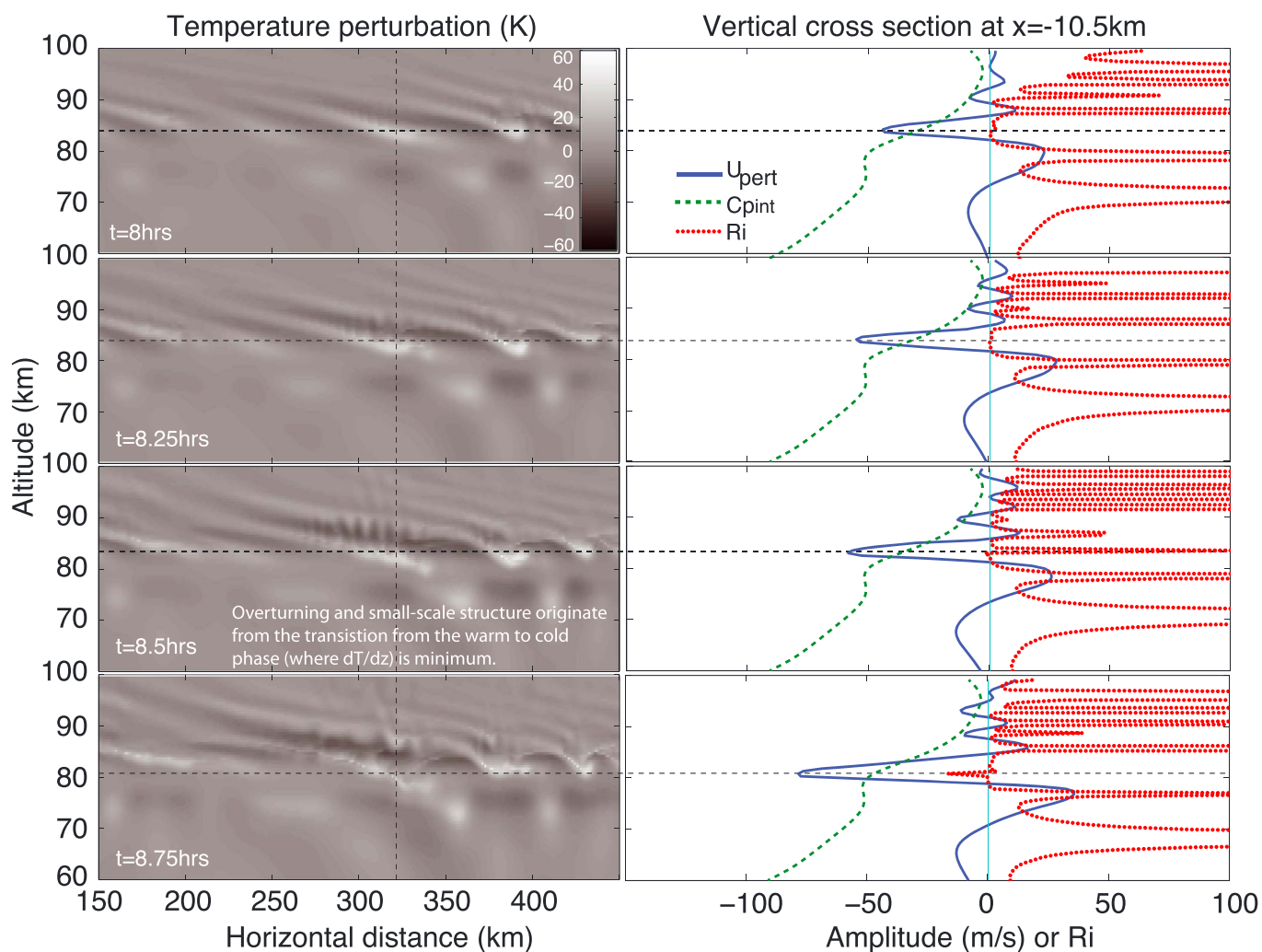


Figure 4. Figure showing the onset of breaking: (left column) the temperature perturbation at four different times, with a vertical dotted black line denoting the location of the vertical cross sections. (right column) The vertical cross section of perturbation velocity, intrinsic phase speed, and Richardson number. The vertical cross section is chosen at a location of initial breaking. The horizontal black line represents the altitude of peak perturbation velocity; the vertical light blue line represents the $Ri = 0.25$ condition.

4.3. Vortex Structures

Figure 5 shows the temperature perturbation at $t = 15$ h enabling the investigation of the scales and spacing of the 2-D vortex structures. In general, the vortices progress downward in time as the wave energy center propagates upward from the source and eventually stall at an altitude of ~ 70 km. Figure 5a shows that the horizontal width and separation of the vortices are 10–20 km and 20–25 km, respectively, with the separations being consistent with observed 25–28 km scales of the small-scale waves identified in *Bossert et al.* [2015]. The vertical scale of the vortices range from 3 to 8 km and are approximately equal to the height over which the Ri is less than 0.25. This is consistent with previous observations of unstable layers [e.g., *Wu and Widdel*, 1991; *Hecht et al.*, 1997; *Lübken*, 1997; *Hoppe et al.*, 1999; *Williams et al.*, 2002]. It is also key to note that while the vortex structures appear most prominent in the warm phase front of the larger-scale wave, the onset of breaking occurs at the boundary between the warm and cold phase, where the perturbation velocity has the largest magnitude. While the largest, most prominent vortices at $z = 70$ km appear mostly stationary, they create a wave-like disturbance in the flow, which progresses westward along the phase fronts of the mountain wave at a speed of ~ 15 m/s as shown in Figure 5b. Therefore, these vortices can generate advecting “wave-like” structure which, along with the vortices themselves, could be interpreted as waves in data obtained by imagers which are subject to layer averaging effects due to integration with altitude.

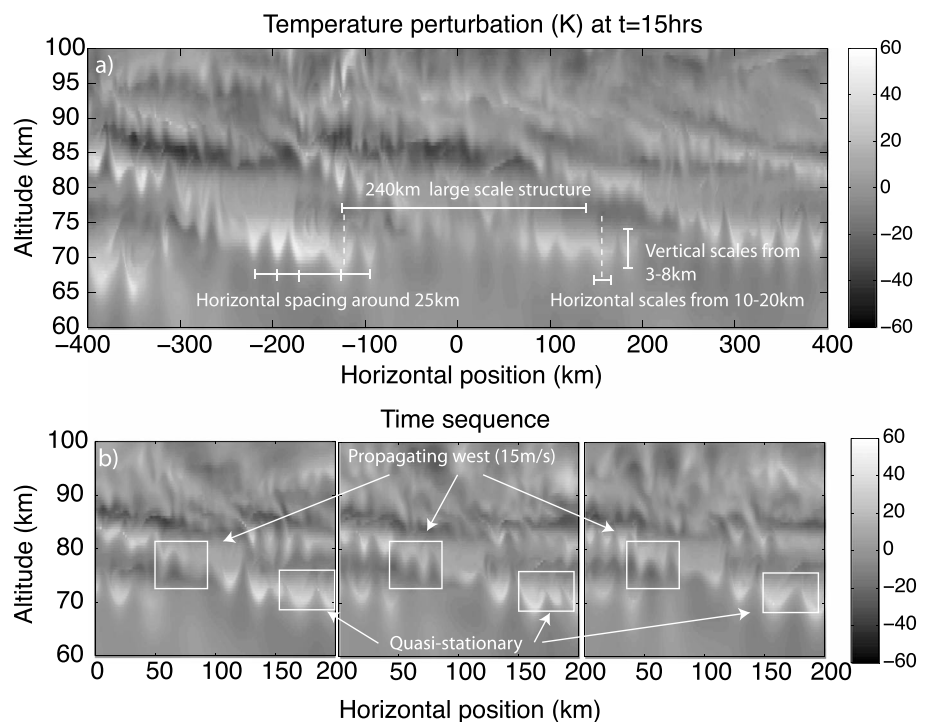


Figure 5. (a) The temperature perturbation at $t = 15$ h, showing the scales or the quasi-stationary vortex structures. (b) A time sequence at $t = 13.3, 13.45,$ and 13.58 h showing the largest stationary vortices producing wave-like disturbances that propagate westward.

5. Evidence for the Tendency Of Small-Scale Structure to Form in the Warm Phase of the Mountain Wave

The two most simple conditions that need to be met for breaking are the convective and/or dynamic instability criteria as mentioned in the previous section. In order to fulfill the linear instability criteria that $u' > = C_{int}$, the perturbation velocity must be large and negative (westward). From the gravity wave polarization relations, the largest westward velocity perturbation coincides with the temperature gradient minimum (the wave is transitioning from the warm to cool phase in altitude), which also minimizes N^2 , driving the Ri number toward negative values. Similarly, the magnitude of the shear is maximized when the temperature is either maximized or minimized, producing a tendency for the Richardson number to fall below one fourth. To illustrate this, we choose a late time in the simulation and plot the altitude at which either of the instability conditions is first met as a function of horizontal position. It is very clear from Figure 6 that this coincides with the warm phase front of the background wave.

Figure 6 shows that the Richardson number has a large negative value near the transition from the hot to cold phase, with the minimum in Ri coinciding with the maximum negative (westward) value of the perturbation velocity. Since the shear term is always positive, the Ri number can only be negative if N^2 is negative. This means that the atmosphere is inherently convectively unstable and may overturn at this point. N^2 will be negative if there is a strong negative temperature gradient which is superadiabatic. Therefore, the combination of a large negative (westward) velocity and shear, coinciding with a strong temperature decrease from its peak (i.e., temperature gradient is minimized), causes both the dynamic and convective instability conditions to be met, leading to inevitable instability. Conversely, when the temperature gradient is maximized (transition from the cold to the hot phase) and the velocity perturbation is positive (eastward), the Ri number is large and stable and neither the convective or dynamic instability conditions are met, as can be seen in Figure 6. Thus, the small-scale features and instabilities form predominantly between the temperature peak (where the velocity shear is maximized) and the minimum in the temperature gradient.

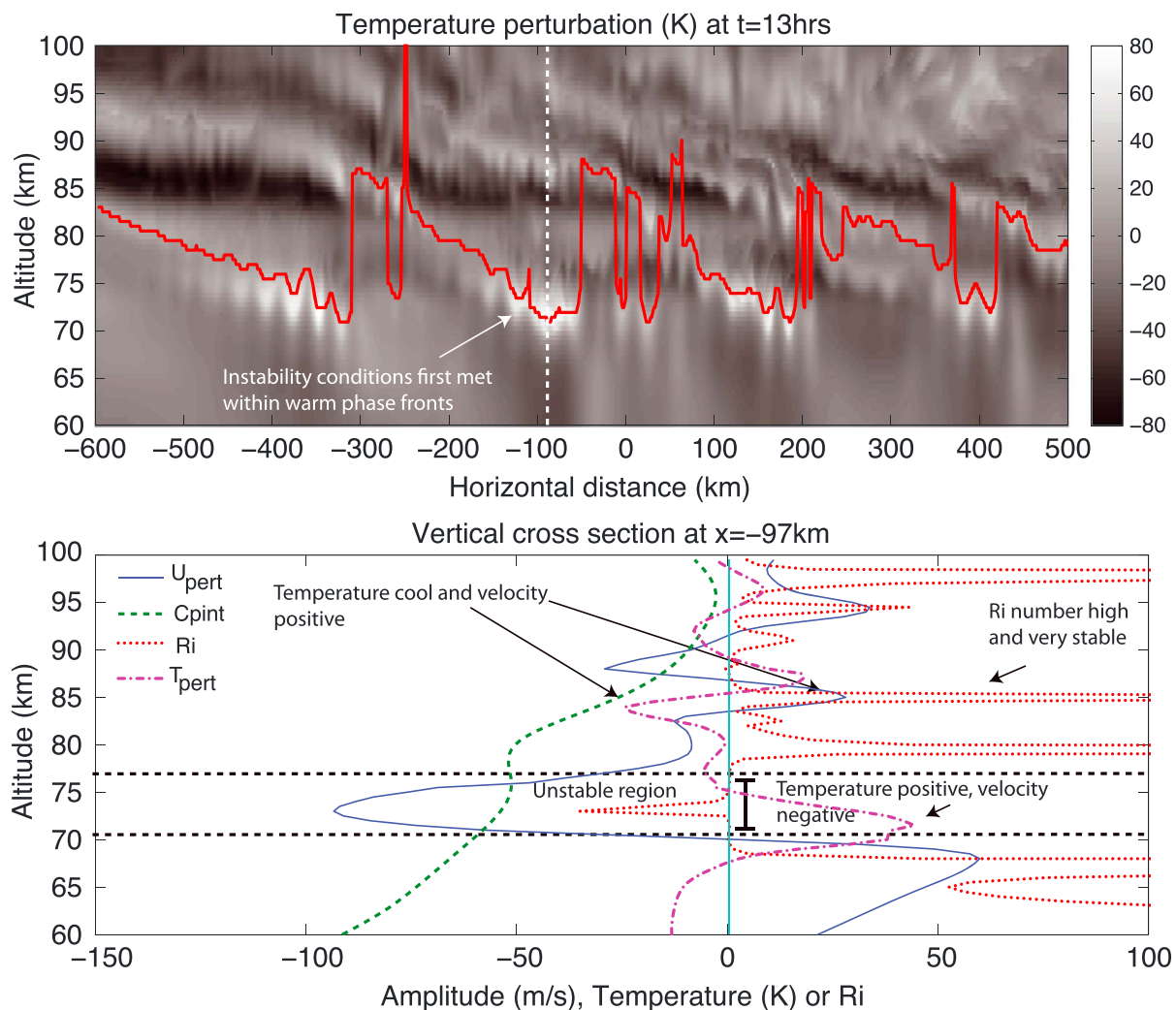


Figure 6. (top) The temperature perturbation at $t = 13$ h. The red line indicates the lowest altitude where an instability condition is first met; the dotted white line indicates the location of the vertical cross section. (bottom) The vertical cross section showing the perturbation horizontal velocity, temperature, Ri , and intrinsic phase speed.

6. In Situ Generation of Small-Scale Structure by the Mountain Wave as Observed Using OH Airglow

The small-scale waves analyzed in *Bossert et al.* [2015] were observed using OH airglow and AMTM data in the OH(3,1) band. To compare, we use the airglow model of *Snively et al.* [2010] and *Snively* [2013] to assess the scales of the small-scale structure seen in the model simulations. *Bossert et al.* [2015] observed small-scale waves which appeared within the warm phase front of the large-scale waves, with horizontal wavelengths between 25 and 28 km, observed phase speeds of 100–130 m/s and amplitudes of 5–7 K.

In Figure 7, we plot the relative temperature response of the OH(3,1) band at 3 times from the onset of breaking. We also plot a spatial wavelet analysis to determine the scales associated with the mountain wave breaking and the horizontal location at which they occur. The wavelet analysis was performed using the method of *Torrence and Compo* [1998] with the default Morlet wavelet function used. We note that the wavelet analysis using this method tends to bias toward larger scales and lower frequencies. Therefore we divide each of the spectral powers by the relevant scale as suggested in *Liu et al.* [2007] and *Chen et al.* [2016]. At $t = 8$ h, instability is beginning to form in the temperature maxima near $x = 100, 300,$ and 400 km horizontal position, with scales of ~ 5 – 10 km. The wavelet analysis is dominated by 40 km–60 km waves predominantly between $x = 100$ and 400 km, which are smaller-scale waves present within the spectrum.

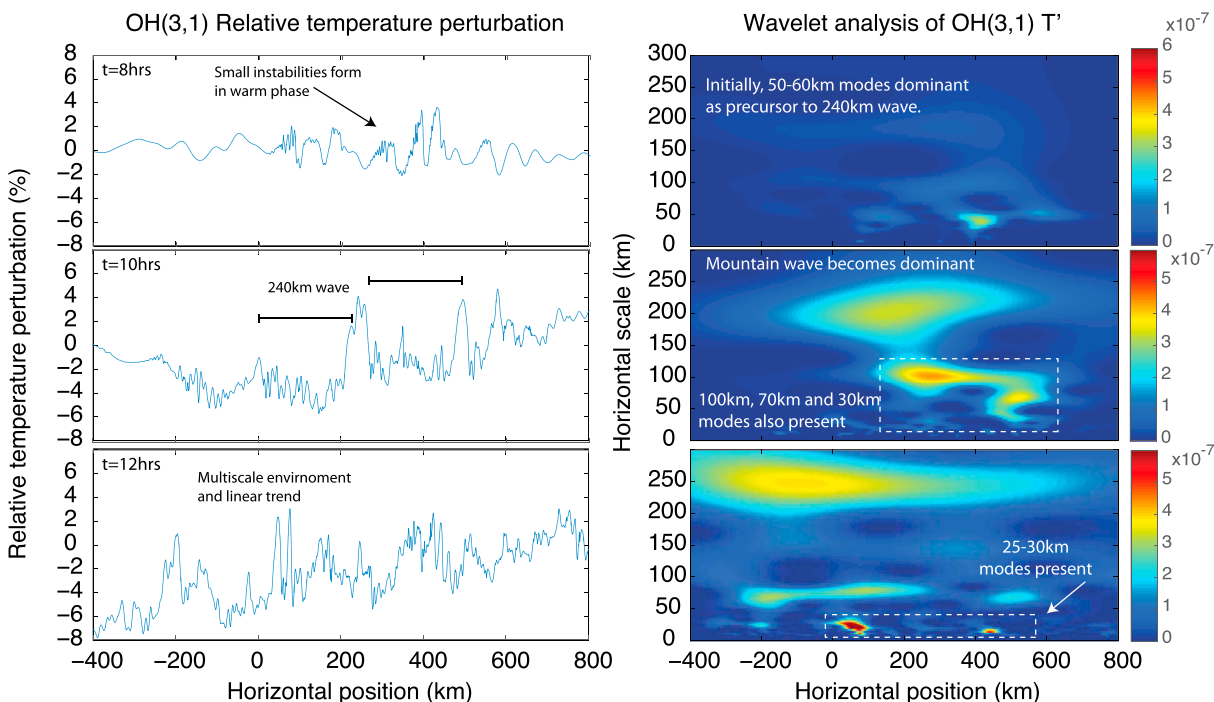


Figure 7. (left column) The OH(3,1) relative temperature airglow response at three separate times. (right column) The corresponding wavelet analysis.

At $t = 10$ h, the mountain wave has propagated up into the MLT and is now the dominant feature in the wavelet analysis, while the relative temperature airglow simulation shows the presence of small-scale structure at all horizontal positions. Several prominent, but localized, modes appear with horizontal scales of 100, 70, and 30 km. While not dominant, there is evidence of nonnegligible 20–30 km horizontal structure within the mountain wave, consistent with the small-scale waves observed in *Bossert et al.* [2015].

At $t = 12$ h, the mountain wave is relatively strong present throughout the length of domain. The simulation evolves into a multiscale environment and smaller-scale structure is present over a horizontal region stretching from $x = -400$ –600km. Once again, there is evidence for 25–30 km modes which are similar to those seen in the AMTM data of *Bossert et al.* [2015].

To investigate the presence of the 20–30 km structures in more detail, we plot the relative temperature airglow response as a function of time and use a Butterworth band-pass filter to isolate structures with horizontal scales between 20 and 30 km. We then multiply the relative response by the average of the background temperature over 79–95 km altitude to get an estimate of the absolute temperature.

Figure 8 shows significant small-scale wave activity concentrated mostly within the warm phase front of the larger-scale wave. Small-scale structure is present within the cold phase also, but the horizontal scale of these structures is less than 20 km. The amplitudes of the 20–30 km small-scale structure are estimated to be between 2 and 6 K; *Bossert et al.* [2015] reported amplitudes ranging from 4 to 7 K; therefore, the results appear consistent. We can also estimate the observed phase speeds of these waves, by estimating the slant of the phase fronts. The majority of the small-scale structures align with the phase of the larger-scale wave. This suggests that they are simply advecting along with the phase of the larger-scale wave. We chose four specific examples to analyze (surrounded by numbered black boxes in Figure 8): (1) This is the largest amplitude small-scale structure in the figure (± 6 K) and is clearly seen even within the warm phase front of the unfiltered data. The structure is present for ~ 2 h and has an estimated observed phase speed of -17 m/s and a horizontal wavelength of ~ 30 km. The phase fronts of the small-scale wave are aligned with the phase front of the large-scale wave and is advecting at the approximate speed but opposite of the background wind. (2) This case is much shorter lived (about 8 min) with a weaker amplitude of ± 4 K and coincides with an incoherent warm front of the mountain wave. The observed phase speed of this wave is faster at -37 m/s and has a slight shorter horizontal wavelength of 28 km. This is likely to be a fast propagating wave or short lived instability. (3) This case provides an example of a quasi-stationary structure, with an amplitude of ± 3 K and horizontal

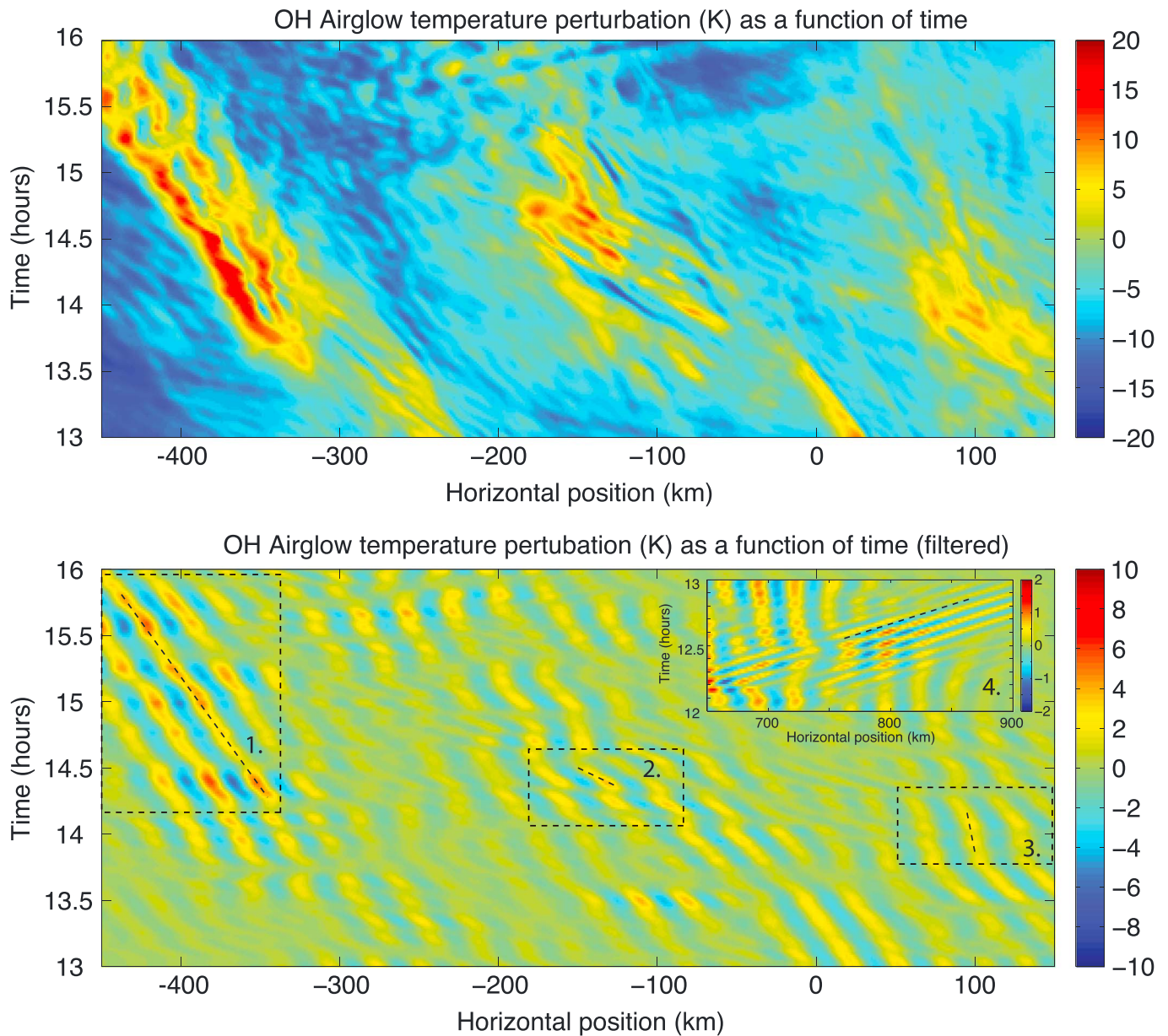


Figure 8. (top) The OH(3,1) temperature perturbation airglow response as a function of time. (bottom) The OH(3,1) airglow response filtered for waves with horizontal scales between 20 and 30 km.

wavelength of 30 km, the phase progresses at only 8 m/s. This is consistent with pass 4 from *Bossert et al.* [2015]. (4) While this case is weak (1 K), it is unique in that it is propagating eastward rather than westward and has an observed phase speed of ~ 106 m/s. This case is consistent with the small-scale propagating waves seen in *Bossert et al.* [2015] passes 1 and 3. In fact, the only waves which propagate eastward are these fast modes. Due to the fast, eastward nature of this wave, it quickly propagates away from the mountain wave and is thus presented in it's own panel in Figure 8.

We note that the majority of the small-scale structures appear wave-like in the simulated airglow response. However, from the x-z plots in previous figures, the structures appear to be the result of instabilities and not propagating GWs. This is consistent with the views of *Hecht* [2004, and references cited within] that structures sometimes interpreted as GWs in airglow images may in fact be instability structures or the result of instabilities. The simulated airglow images give no insight or indication of the vortices which are present in the

x-z simulation results and could easily be misinterpreted as GW structures without correlative data or modeling. The simulation shows that some small-scale wave-like features seen in the data could be evidence for instability/breaking in situ of the larger-scale wave.

7. Summary and Conclusions

We have used a 2-D compressible, nonlinear numerical model to simulate a large-amplitude, stationary mountain wave observed over Mount Cook, NZ, and documented in Bossert *et al.* [2015]. The wave was observed to have small-scale waves ($\lambda_x = 25\text{--}28$ km) propagating within the warm phases of the mountain wave and to decrease rapidly in amplitude above 85 km. This study motivated by three questions that arose from this event: (1) What mechanism causes the rapid decrease in amplitude above 85 km, and how does this manifest itself for stationary mountain waves? (2) Why do the small-scale waves appear to have a preference for the warm phase front of the larger-scale wave? (3) Can the small-scale waves seen in the data be explained by in situ generation by the larger-scale wave?

Numerical model results find that the rapid amplitude decrease is due to breaking and instability, leading to large-amplitude, almost-stationary vortices forming initially on the boundary between the warm and cool phases of the mountain wave that manifest primarily along the warm phase front. These vortices are roughly 20–25 km apart and 3–8 km in height, and both the convective and dynamic instability conditions are met in these regions, and the scales are approximately equal to the depth of the unstable region. We note however that these results are limited to 2-D breaking only and that amplitudes may be somewhat overestimated, especially at later times.

There is a definite preference for the convective and shear instability conditions to be first met within the warm phase of the modeled mountain wave. With increasing altitude, the shear instability condition is first met where the wave's perturbation velocity shear and temperature are maximized, with a convectively unstable region occurring where the westward perturbation velocity is maximized and the temperature gradient is minimized.

Using the model's capabilities to simulate the OH(3,1) airglow response to the mountain wave, we find the presence of 20–30 km horizontal structures predominantly within, and aligned with, the warm phase of the mountain wave as consistent with those observed in Bossert *et al.* [2015]. The simulation suggests that most of the small-scale structure are advecting with the phase fronts of the large-scale waves and are generated in situ by the mountain wave as a result of instabilities and breaking. It is noted that the airglow results alone give no clear indication that the vortex structures seen in the full 2-D simulation are not waves, and it would be easy to misinterpret the simulated airglow response as waves rather than instabilities if only OH airglow data were available. This highlights the importance of using complementary instruments and models to interpret observations.

Acknowledgments

Research by C. J. Heale and J. B. Snively was supported under NSF grants AGS-1151746 and AGS-1344356. Research by D. C. Fritts and K. Bossert was supported under NSFAGS-13386484 and AGS-1524598. The development of the GV AMTM was funded by the NSF grant AGS-1061892. The DEEPWAVE campaign was sponsored by the NSF grant AGS-1338666 (USU). Copies of the simulation data and figures can be obtained on request to the authors at healec@erau.edu.

References

- Achatz, U. (2007), Gravity-wave breaking: Linear and primary nonlinear dynamics, *Adv. Space Res.*, *40*, 719–733.
- Andreassen, Ø., C.-E. Wasberg, D. C. Fritts, and J. R. Isler (1994), Gravity wave breaking in two and three dimensions: 1. Model description and comparison of two-dimensional evolutions, *J. Geophys. Res.*, *99*, 8095–8108.
- Bale, D. S., R. J. LeVeque, S. Mitran, and J. A. Rossmannith (2002), A wave propagation method for conservation laws and balance laws with spatially varying flux functions, *J. Sci. Comput.*, *24*(3), 955–978.
- Bossert, K., et al. (2015), Momentum flux estimates accompanying multiscale gravity waves over Mount Cook, New Zealand, on 13 July 2014 during the DEEPWAVE campaign, *J. Geophys. Res. Atmos.*, *120*, 9323–9337, doi:10.1002/2015JD023197.
- Chen, C., X. Chu, J. Zhao, B. R. Roberts, Z. Yu, W. Fong, X. Lu, and J. A. Smith (2016), Lidar observations of persistent gravity waves with periods of 3–10 h in the Antarctic middle and upper atmosphere at McMurdo (77.83°S, 166.67°E), *J. Geophys. Res. Space Physics*, *121*, 1483–1502, doi:10.1002/2015JA022127.
- Dosser, H. V., and B. R. Sutherland (2011), Anelastic internal wave packet evolution and stability, *J. Atmos. Sci.*, *68*, 2844–2859.
- Drob, D. P., et al. (2008), An empirical model of the Earth's horizontal wind fields: HWM07, *J. Geophys. Res.*, *113*, A12304, doi:10.1029/2008JA013668.
- Dunkerton, T. J. (1989), Theory of internal gravity wave saturation, *Pure Appl. Geophys.*, *130*, 373–397.
- Espy, P. J., G. O. L. Jones, G. R. Swenson, J. Tang, and M. J. Taylor (2004), Seasonal variations of the gravity wave momentum flux in the Antarctic mesosphere and lower thermosphere, *J. Geophys. Res.*, *109*, D23109, doi:10.1029/2003JD004446.
- Espy, P. J., R. E. Hibbins, G. R. Swenson, J. Tang, M. J. Taylor, D. M. Riggan, and D. C. Fritts (2006), Regional variations of mesospheric gravity-wave momentum flux over Antarctica, *Ann. Geophys.*, *24*, 81–88, doi:10.5194/angeo-24-81-2006.
- Franke, P. M., and W. A. Robinson (1999), Nonlinear behavior in the propagation of atmospheric gravity waves, *J. Atmos. Sci.*, *56*, 3010–3027.
- Fritts, D., and M. J. Alexander (2003), Gravity wave dynamics and effects in the middle atmosphere, *Rev. Geophys.*, *41*(1), 1003, doi:10.1029/2001RG000106.
- Fritts, D. C. (1984), Gravity wave saturation in the middle atmosphere: A review of theory and observations, *Rev. Geophys.*, *22*, 275–308.

- Fritts, D. C., and T. J. Dunkerton (1985), Fluxes of heat and constituents due to convectively unstable gravity waves, *Ann. Geophys.*, *68*, 247–265.
- Fritts, D. C., and W. Lu (1993), Spectral estimates of gravity wave energy and momentum fluxes. II: Parameterization of wave forcing and variability, *J. Atmos. Sci.*, *50*, 3695–3713.
- Fritts, D. C., and T. S. Lund (2011), Gravity wave influences in the thermosphere and ionosphere: Observations and recent modeling, in *Aeronomy of the Earth's Atmosphere and Ionosphere*, edited by M. A. Abdu and D. Pancheva, pp. 109–130, Springer, Netherlands.
- Fritts, D. C., and R. Vincent (1987), Mesospheric momentum flux studies at Adelaide, Australia, *J. Atmos. Sci.*, *44*, 605–619.
- Fritts, D. C., J. F. Garten, and O. Andreasson (1996), Wave breaking and transition to turbulence in stratified shear flows, *J. Atmos. Sci.*, *53*, 1057–1085.
- Fritts, D. C., S. L. Vadas, K. Wan, and J. A. Werne (2006), Mean and variable forcing of the middle atmosphere by gravity waves, *J. Atmos. Sol. Terr. Phys.*, *68*, 247–265.
- Fritts, D. C., L. Wang, J. Werne, T. Lund, and K. Wan (2009), Gravity wave instability and dynamics at high Reynolds numbers. Part I: Wave field evolution at large amplitudes and high frequencies, *J. Atmos. Sci.*, *66*, 1126–1148, doi:10.1175/2008JAS2726.1.
- Fritts, D. C., P.-D. Pautet, K. Bossert, M. J. Taylor, B. P. Williams, H. Limura, T. Yuan, N. J. Mitchell, and G. Stober (2014), Quantifying gravity wave momentum fluxes with mesosphere temperature mappers and correlative instrumentation, *J. Geophys. Res. Atmos.*, *119*, 13,583–13,603, doi:10.1002/2014JD022150.
- Fritts, D. C., B. Laughman, T. S. Lund, and J. B. Snively (2015), Self-acceleration and instability of gravity wave packets: 1. Effects of temporal localization, *J. Geophys. Res. Atmos.*, *120*, 8783–8803, doi:10.1002/2015JD023363.
- Fritts, D. C., et al. (2016), The Deep Propagating Gravity Wave Experiment (DEEPWAVE): An airborne and ground-based exploration of gravity wave propagation and effects from their sources throughout the lower and middle atmosphere, *Bull. Am. Meteorol. Soc.*, *97*, 425–453, doi:10.1175/BAMS-D-14-00269.1.
- Garcia, R. R., and S. Solomon (1985), The effect of breaking gravity waves on the dynamics and chemical composition of the mesosphere and lower thermosphere, *J. Geophys. Res.*, *90*, 3850–3868.
- Gardner, C. S., and A. Z. Liu (2007), Seasonal variations of the vertical fluxes of heat and horizontal momentum in the mesopause region at Starfire Optical Range, New Mexico, *J. Geophys. Res.*, *112*, D09113, doi:10.1029/2005JD006179.
- Gossard, E. E., and W. H. Hooke (1975), *Waves in the Atmosphere*, Elsevier, 456 pp., New York.
- Heale, C. J., J. B. Snively, and M. P. Hickey (2014a), Numerical simulation of the long range propagation of gravity wave packets at high latitudes, *J. Geophys. Res. Atmos.*, *119*, 11,116–11,134, doi:10.1002/2014JD022099.
- Heale, C. J., J. B. Snively, M. P. Hickey, and C. J. Ali (2014b), Thermospheric dissipation of upward propagating gravity wave packets, *J. Geophys. Res. Atmos.*, *119*, 3857–3872, doi:10.1002/2013JA019387.
- Hecht, J. H. (2004), Instability layers and airglow imaging, *Rev. Geophys.*, *42*, RG1001, doi:10.1029/2003RG000131.
- Hecht, J. H., R. L. Walterscheid, D. C. Fritts, J. R. Isler, D. C. Senft, C. S. Gardner, and S. J. Franke (1997), Wave breaking signatures in OH airglow and sodium densities and temperatures. Part I: Airglow imaging, Na lidar, and MF radar observations, *J. Geophys. Res.*, *102*, 6655–6668.
- Hickey, M. P., R. L. Walterscheid, and G. Schubert (2011), Gravity wave heating and cooling of the thermosphere: Sensible heat flux and viscous flux of kinetic energy, *J. Geophys. Res.*, *116*, A12326, doi:10.1029/2011JA016792.
- Hitchman, M. H., K. W. Bywaters, D. C. Fritts, L. Coy, E. Kudeki, and F. Surucu (1992), Mean winds and momentum fluxes over Jicamarca, Peru, during June and August 1897, *J. Atmos. Sci.*, *49*, 2372–2383.
- Hocke, K., and T. Tsuda (2001), Gravity waves and ionospheric irregularities over tropical convection zones observed by GPS/MET radio occultation, *Geophys. Res. Lett.*, *28*, 2815–2818.
- Holton, J. R. (1982), The role of gravity wave induced drag and diffusion in the momentum budget of the mesosphere, *J. Atmos. Sci.*, *39*, 791–799.
- Holton, J. R. (1983), The influence of gravity wave breaking on the general circulation of the middle atmosphere, *J. Atmos. Sci.*, *40*, 2497–2507.
- Hoppe, U.-P., T. Eriksen, E. V. Thrane, T. A. Blix, J. Fiedler, and F.-J. Lübken (1999), Observations in the polar middle atmosphere by rocket-borne Rayleigh lidar: First results, *Earth Planets Space*, *51*, 815–824.
- Hung, R. J., and J. P. Kuo (1978), Ionospheric observations of gravity-waves associated with hurricane Eloise, *J. Geophys. Res.*, *45*, 67–80.
- Kelley, M. C. (1997), In situ ionospheric observations of severe weather-related gravity waves and associated small-scale plasma structure, *J. Geophys. Res.*, *102*, 329–336.
- Klostermeyer, J. (1991), Two- and three-dimensional parametric instabilities in finite amplitude internal gravity waves, *Geophys. Astrophys. Fluid Dyn.*, *64*, 1–25.
- LeVeque, R. J. (2002), *Finite Volume Methods for Hyperbolic Problems*, *Cambridge Texts in Appl. Math.*, Cambridge Univ. Press, Cambridge, New York.
- LeVeque, R. J., and M. J. Berger (2004), Clawpack software version 4.6. [Available at <http://www.clawpack.org>.]
- Lindzen, R. S. (1981), Turbulence and stress owing gravity wave and tidal breakdown, *J. Geophys. Res.*, *86*(C10), 9707–9714.
- Liu, X., J. Xu, H. L. Liu, J. Yue, and W. Yuan (2014), Simulations of large winds and wind shears induced by gravity wave breaking in the mesosphere and lower thermosphere (MLT) region, *Ann. Geophys.*, *32*, 543–552, doi:10.5194/angeo-32-543-2014.
- Liu, Y., X. S. Liang, and R. H. Weisberg (2007), Rectification of the bias in the wavelet power spectrum, *J. Atmos. Oceanic Technol.*, *24*(12), 2093–2102.
- Lübken, F.-J. (1997), Seasonal variations of turbulent energy dissipation rates at high latitudes as determined by in situ measurements of neutral density fluctuations, *J. Geophys. Res.*, *102*, 13,441–13,456.
- Lübken, F. J., M. J. Jarvis, and G. O. L. Jones (1999), First in situ temperature measurements at the Antarctic summer mesopause, *Geophys. Res. Lett.*, *26*(24), 3581–3584.
- Lund, T. S., and D. C. Fritts (2012), Numerical simulation of gravity wave breaking in the lower thermosphere, *J. Geophys. Res.*, *117*, D21105, doi:10.1029/2012JD017536.
- Nakamura, T., T. Tsuda, M. Yamamoto, S. Fukao, and S. Kato (1993), Characteristics of gravity waves in the mesosphere observed with the middle and upper atmosphere radar: 1. Momentum Flux, *J. Geophys. Res.*, *98*, 8899–8910.
- Nakamura, T., A. Higashikawa, T. Tsuda, and V. Matsushita (1999), Seasonal variations of gravity wave structures in OH airglow with a CCD imager at Shigaraki, *Earth Planets Space*, *51*, 897–906.
- Picone, J. M., A. E. Hedin, D. P. Drob, and A. Aikin (2002), NRL-MSISE-00 empirical model of the atmosphere: Statistical comparisons and scientific issues, *J. Geophys. Res.*, *107*(A12), 1468, doi:10.1029/2002JA009430.
- Pitteway, M. L. V., and C. O. Hines (1963), The viscous damping of atmospheric gravity waves, *Can. J. Phys.*, *41*, 1935–1948.
- Snively, J., V. Pasko, and M. Taylor (2010), OH and OI airglow layer modulation by ducted short-period gravity waves: Effects of trapping altitude, *J. Geophys. Res.*, *115*, A11311, doi:10.1029/2009JA015236.

- Snively, J. B. (2013), Mesospheric hydroxyl airglow signatures of acoustic and gravity waves generated by transient tropospheric forcing, *Geophys. Res. Lett.*, *40*, 4533–4537, doi:10.1002/grl.50886.
- Snively, J. B., and V. P. Pasko (2008), Excitation of ducted gravity waves in the lower thermosphere by tropospheric sources, *J. Geophys. Res.*, *113*, A06303, doi:10.1029/2007JA012693.
- Sonmor, L. J., and G. P. Klaassen (1997), Toward a unified theory of gravity wave stability, *J. Atmos. Sci.*, *54*, 2655–2678.
- Swenson, G. R., R. Haque, W. Yang, and C. S. Gardner (1999), Momentum and energy fluxes of monochromatic gravity waves observed by an OH imager at Starfire Optical Range, New Mexico, *J. Geophys. Res.*, *104*(D6), 6067–6080.
- Taylor, M. J., W. R. Pendleton Jr., S. Clark, H. Takahashi, D. Gobbi, and R. A. Goldberg (1997), Image measurements of short-period gravity waves at equatorial latitudes, *J. Geophys. Res.*, *102*, 26,283–26,299.
- Torrence, C., and G. P. Compo (1998), A practical guide to wavelet analysis, *Bull. Am. Meteorol. Soc.*, *79*(1), 61–78.
- Tsuda, T., Y. Murayama, M. Yamamoto, S. Kato, and S. Fukao (1990), Seasonal variation of momentum flux in the mesosphere: Seasonal variation of momentum flux in the mesosphere observed with the MU radar, *Geophys. Res. Lett.*, *17*, 725–728.
- Vadas, S. L. (2007), Horizontal and vertical propagation and dissipation of gravity waves in the thermosphere from lower atmospheric and thermospheric sources, *J. Geophys. Res.*, *112*, A06305, doi:10.1029/2006JA011845.
- Vadas, S. L., and D. C. Fritts (2006), Influence of solar variability on gravity wave structure and dissipation in the thermosphere from tropospheric convection, *J. Geophys. Res.*, *111*, A10512, doi:10.1029/2005JA011510.
- Vadas, S. L., and H. L. Liu (2009), Generation of large-scale gravity waves and neutral winds in the thermosphere from the dissipation of convectively generated gravity waves, *J. Geophys. Res.*, *114*, A10310, doi:10.1029/2009JA014108.
- Vadas, S. L., and H. L. Liu (2013), Numerical modeling of the large-scale neutral and plasma responses to the body forces created by the dissipation of gravity waves from 6 h of deep convection in Brazil, *J. Geophys. Res. Space Physics*, *118*, 2593–2617, doi:10.1002/jgra.50249.
- Vincent, R. A., and I. M. Reid (1983), HF Doppler measurements of mesospheric momentum fluxes, *J. Atmos. Sci.*, *40*, 1321–1333.
- Waterscheid, R. L., and M. P. Hickey (2011), Group velocity and energy flux in the thermosphere: Limits on the validity of group velocity in a viscous atmosphere, *J. Geophys. Res.*, *116*, D12101, doi:10.1029/2010JD014987.
- Williams, B. P., M. A. White, D. A. Krueger, and C. Y. She (2002), Observation of a large amplitude wave and inversion layer leading to convective instability in the mesopause region over Fort Collins, CO (41°N, 105°W), *Geophys. Res. Lett.*, *29*(19), 1850, doi:10.1029/2001GL014514.
- Wu, Y. F., and H. U. Widdel (1991), Further study of a saturated gravity wave spectrum in the mesosphere, *J. Geophys. Res.*, *96*, 9263–9272.
- Yiğit, E., A. D. Aylward, and A. S. Medvedev (2008), Parameterization of the effects of vertically propagating gravity waves for thermosphere general circulation models: Sensitivity study, *J. Geophys. Res.*, *113*, D19106, doi:10.1029/2008JD010135.
- Yiğit, E., A. S. Medvedev, A. D. Aylward, P. Hartogh, and M. J. Harris (2009), Modeling the effects of gravity wave momentum deposition on the general circulation above the turbopause, *J. Geophys. Res.*, *114*, D07101, doi:10.1029/2008JD011132.